UKAEA-CCFE-PR(23)164

M. Fontana, G. Giruzzi, F. P. Orsitto, E. de la Luna, R. Dumont, L. Figini, D. Kos, M. Maslov, S. Schmuck, L. Senni, C. Sozzi, C. Challis, D. Frigione, J. Garcia, L. Garzotti, J. Hobirk, A. Kappatou, D. Keeling, E. Lerche, C. Maggi, J. Mailloux, F. Rimini, D. Van Eester

Investigation of Te measurements discrepancies between ECE and Thomson diagnostics in high-performance plasmas in JET

Investigation of Te measurements discrepancies between ECE and Thomson diagnostics in high-performance plasmas in JET

M. Fontana, G. Giruzzi, F. P. Orsitto, E. de la Luna, R. Dumont, L. Figini, D. Kos, M. Maslov, S. Schmuck, L. Senni, C. Sozzi, C. Challis, D. Frigione, J. Garcia, L. Garzotti, J. Hobirk, A. Kappatou, D. Keeling, E. Lerche, C. Maggi, J. Mailloux, F. Rimini, D. Van Eester

This is a preprint of a paper submitted for publication in Nuclear Fusion

High T_e discrepancies between ECE and Thomson diagnostics in high-performance JET discharges

M. Fontana,[1] G. Giruzzi,[2] F. P. Orsitto,[3] E. de la Luna,[4] R. Dumont,[2] L. Figini,[5] D. Kos,[1] M. Maslov,[1] S. Schmuck,[5] L. Senni,[6] C. Sozzi,[5] D. Frigione,[3] J. Garcia,[2] L. Garzotti,[1] J. Hobirk,[7] A. Kappatou,[7] D. Keeling,[1] E. Lerche,[1] F. Rimini,[1] D. van Eester,[8] C. F. Maggi,[1] J. Mailloux,[1] and JET contributors[a)]

[1)] *United Kingdom Atomic Energy Authority, Culham Centre for Fusion Energy, Culham Science Centre, Abingdon, Oxon, OX14 3DB, UK*
[2)] *CEA, IRFM F-13108 Saint Paul-lez-Durance, France*
[3)] *ENEA Department Fusion and Technology for Nuclear Safety, C R Frascati , 00044 Frascati, Italy*
[4)] *National Fusion Laboratory, CIEMAT, Madrid, Spain*
[5)] *Istituto per la Scienza e Tecnologia dei Plasmi, CNR, 20125 Milano, Italy*
[6)] *CNR Institute for applied mathematics Mauro Picone (IAC), Via dei Taurini, 19, 00185 Roma, Italy*
[7)] *Max-Planck-Institut für Plasmaphysik, D-85748 Garching, Germany*
[8)] *Laboratory for Plasma Physics, LPP-ERM/KMS, Brussels, Belgium*

(*matteo.fontana@ukaea.uk)

(Dated: 27 September 2023)

The present paper is dedicated to the study of the discrepancies encountered in electron temperatures (T_e) measurements carried out with Electron Cyclotron Emission (ECE) and Thomson Scattering (TS) diagnostics in the core of the JET tokamak. A large database of discharges has been collected, including high-performance scenarios performed with Deuterium only and Deuterium-Tritium mixtures. Discrepancies have been found between core T_e measurements taken with an X-mode ECE interferometer (T_{ECE}) and a LIDAR TS system (T_{LID}) for $T_e > 5$ keV. Depending on the plasma scenario, T_{ECE} has been found to be systematically higher or lower than T_{LID}. Discrepancies have also been observed between the peaks of the ECE spectrum in the second (X2) and third (X3) harmonic domains, even in high optical thickness conditions. These discrepancies can be interpreted as evidence of the presence of non-Maxwellian features in the electron energy distribution function (EEDF). In order to investigate the relation between the shape of the EEDF and the measured discrepancies, a model for bipolar perturbations of Maxwellian EEDF has been developed. The model allows analytical calculations of ECE absorption and emission coefficients, hence the comparison of modelled ECE spectra with experimental data. The different experimental results observed for the various JET scenarios have been found to be qualitatively reproducible by adapting the model parameters, suggesting that bipolar distortions of the bulk EEDF could play a role in giving rise to the reported discrepancies between ECE and TS measurements.

I. INTRODUCTION

Reliable and precise measurements of the electron temperature (T_e) in a fusion plasma experiment represent a necessary condition both for contemporary research and for future reactor-like devices including commercial facilities. Some of the most used techniques for measuring electron temperature in the plasma core are Electron cyclotron emission (ECE)[1] and incoherent Thomson scattering (TS)[2]. They have been used in most of tokamaks and stellarators in the last several decades. In spite of the large body of experience accumulated in the use of these techniques, discrepancies between their T_e measurements have been reported in high temperature tokamak plasmas in multiple machines.

The discrepancies in question were first observed in the 1990s on TFTR[3,4] and on JET[5]. On both machines, the core electron temperature measurements taken using ECE were found to be up to 20% higher than those taken with TS at high temperatures (T_e>5 keV). This was observed in pulses heated with neutral beam injection (NBI) and ion cyclotron resonance heating (ICRH). In 2004, at JET, core ECE temperatures, calculated from the second harmonic domain of the extraordinary mode ECE spectrum (X2), were found to be higher than their TS counterparts, when in core T_e was high enough (T_e>5 keV). On the contrary, core temperatures deduced from the third harmonic domain (X3) remained in good agreement with the TS measurements when the optical thickness was sufficiently large ($\tau_{X3} > 3$). This was unexpected, since the radiation temperature measured with second and third harmonics should match well if the plasma is optically thick and it is considered that the electron energy distribution function (EEDF) is Maxwellian. This mismatch was interpreted as a hint of the possible presence of non-Maxwellian features in the EEDF, which would affect the T_e measurements obtained from different ECE harmonics in different ways. In 2006, very similar experiments to those of 2004 were repeated at JET where the H concentration was increased from 3% (in 2004) to 8% (in 2006) in order to reduce ion losses and consequently the risk of damage to the vessel walls. No discrepancy between ECE and TS nor differences

[a)] See the author list of 'Overview of JET results for optimising ITER operation' by J. Mailloux et al. to be published in Nuclear Fusion Special issue: Overview and Summary Papers from the 28th Fusion Energy Conference (Nice, France, 10-15 May 2021) between peak X2 and X3 ECE measurements were observed in those cases[6,7]. The impact of the different H concentration on the distribution functions of the resonating ions was evaluated using the PION code[8], which considers the effects of ICRH coupling to the neutral beam generated fast deuteron population. This analysis showed a clear reduction in the temperature of a small population of high-energy hydrogen ions with the increased H concentration[6]. It is reasonable to assume that the interaction between the hydrogen ions and the electrons led to different effects on the EEDF in the two cases.

Conflicting evidence was found at other tokamaks. At Alcator C-mod, a study reported comparable ECE and TS temperature measurements up to $T_e = 8$ keV. The plasmas in these experiments were heated using exclusively ICRH in different configurations[9]. The results of this work seem to indicate that the discrepancies might not just be caused by high T_e, but other factors could be playing a role. In other experiments at FTU, it was instead observed that, for very high temperatures ($T_e > 14$ keV) TS measurements were found to reach values up to 50% higher than ECE ones, opposite to what had previously been observed in JET and TFTR. The discrepancies appeared for core electron temperatures $T_e > 8$ keV, while the two measurements generally agreed for lower temperatures. These experiments exclusively used EC waves for heating[10].

It is well known that the ECE spectrum is disturbed by the presence of suprathermal electrons, such as those generated during lower hybrid current drive(LHCD) experiments. In the case of perpendicular observation, this typically results in enhanced emission measured on the low field side, optically thin part of the ECE spectrum[11]. It was suggested[12,13] that the differences in measurements, combined with the atypical ECE spectra, could be related to a deformation of the EEDF in the core of the plasma, specifically around energies close to the thermal energy of the electrons. In fact, distortions of the EEDF would affect differently ECE and TS measurements due to the fact that the two diagnostics operate based on different principles. ECE measurements in particular are sensitive to the first derivative of the distribution function, for energies close to the thermal energy, through the expression of the absorption coefficient[14]. For the cases in TFTR and JET where discrepancies have been observed, the heating methods employed (NBI, ICRH), do not directly affect the electrons distribution as it happens instead when LHCD is used. Here, we hypothesize that the effects on the EEDF might be caused by the interaction of the electrons with a population of energetic ions generated by auxiliary heating (neutral beam or ion cyclotron heating), or with high-energy α particles, products of D-T fusion.

In particular, there are several mechanisms that, in the presence of fast ions, can result in low-amplitude bipolar deformation of the EEDF . Two examples of these are collisional relaxation[15] and Landau damping of kinetic Alfvén waves[16,17].

After the installation of the ITER-like wall[18], one of the goals of JET was the development of high-performance plasma scenarios. In 2021, these scenarios have been further studied in D-T plasmas[19], in a set of experiments during which a new record in generated fusion energy was achieved[20]. The D-T campaign represented a unique chance to continue the study of the differencies between ECE and TS measurements. With this goal, the values of central T_e from 246 JET discharges, from 2019 to 2022, have been gathered in a large dataset that includes a large range of conditions for D and D-T plasmas. For the high-temperature plasmas (T_e>5 keV) included in this database, various cases were found in which ECE measurements were found to be higher or lower than TS ones, depending on the plasma scenario. Furthermore, broadband ECE X-mode spectra detected by the JET Martin-Puplett interferometer display differences between 2$^{\text{nd}}$ and 3$^{\text{rd}}$ harmonics even when the latter is optically thick.

In order to perform a systematic analysis of these discrepancies, a model was developed for bipolar distortions of a Maxwellian EEDF. These perturbed distribution functions allow analytic calculations of the emission and absorption coefficients for electron cyclotron emission, from which the radiative temperature that would be observed by an ECE diagnostic is predicted. These predictions are then compared with measurements to judge the capabilities of the model to qualitatively reproduce observations.

In section II, the assembled JET database will be introduced, including a description of the ECE and TS diagnostics available at JET and the specific scenarios included in the pulse selection. The T_e measurements included in the database are discussed and compared in section III. Section IV introduces the model for the bipolar distortion of the EEDF and section V compares its predictions with the experimental observations. Finally, section VI recaps the contents of this paper and mentions some of the next steps in studying this database. Appendix A contains the formulas used for the calculation of the absorption and emission coefficients for ECE.

II. CONSTRUCTION OF DATABASE

In order to continue the study of the discrepancies between ECE and TS measurements, a large database of electron temperature measurements from JET has been assembled from a variety of experiments from 2019 to 2022. In this section, the characteristics of JET core T_e diagnostics are presented, followed by a description of the scenarios and pulses included in the database.

A. ECE and Thomson diagnostics at JET

There are two Thomson scattering diagnostic systems at JET: the high resolution system (HRTS)[21,22] and a LIDAR system[23–25].The two systems have independent calibration procedures. LIDAR provides electron density and electron temperature profiles measured at the plasma low-field side (LFS), and at the high-field side (HFS) partially. The laser pulses are repeated at a frequency of 4 Hz; radial spatial resolution is of the order of 7 cm. HRTS has a better repetition rate (20 Hz) and radial resolution (2 cm), allowing good pedestal profile measurements. Owing to its line of sight (see figure

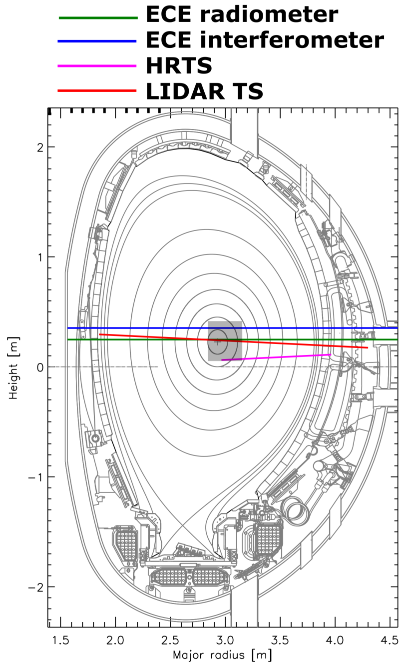

FIG. 1: Electron temperature diagnostics at JET: geometry of observation. The gray square represents the horizontal range for averaging used to calculate T_{LID} and T_{ECE}

.

1), HRTS does not cover the region around the magnetic axis and it is is limited to the LFS profile only (ρ>0.2, ρ being the normalised radius). For this reason, in the following, HRTS will not be considered and only the LIDAR measurements of the central temperature will be used.

The ECE measurements are provided by two interferometers (for ordinary and extraordinary modes) of the Martin-Puplett type[26] and a heterodyne radiometer[27] observing the plasma through horizontal lines of sight perpendicular to the magnetic field lines along the major radius, close to the vessel midplane (see figure 1). The lines of sight of the two interferometers contain, at the vessel exit, a polariser that selects ordinary and extraordinary mode respectively. Absolute calibration of the interferometers is obtained placing a black-body source (covering the range 50-500 GHz and reaching up to 873 K) inside the vessel. The heating plate of the source is made of stainless steel and a movable lid covered with Thomas Keating THz RAM (Radar Absorbing Material) can be controlled remotely to cover it, alternating high and intermediate temperatures during the calibration. More details on the sources and on the calibration procedures can be found in the literature[26]. The radiometer is instead calibrated against the interferometers profiles on a pulse-by-pulse basis, usually during the B-field ramp-up phase. The interferometers measurements are acquired at a frequency of 60 Hz at both LFS and HFS, limited by cutoff for the O-mode and 2^{nd}-3^{rd} harmonics overlapping for the X-mode. The spatial resolution around the plasma centre is about 10 cm. For the O-mode interferometer, the core of most of the high performance pulses, except for the ones with the highest B_t, was found to be in cutoff, so its measurements have not been considered in this study. The 96-channel ECE radiometer has the advantage of a high temporal resolution. However, such resolution, much higher than the LIDAR, is not useful for this study; moreover, the radiometer is cross-calibrated on the interferometer. For these reasons, the radiometer has not been used in this work.

1. Notes on diagnostics calibration stability

When looking at data collected over more than three years, the consistency of the diagnostics calibration becomes a matter of great importance. For the ECE interferometer, given the complications arising in organising in-vessel calibrations, the stability of the calibration is also monitored more regularly using two different methods. First is the local calibration of the instrument back-end as described in section IV.C of[26]. A pair of black body-like sources (Thomas Keating THz RAM, as for the in-vessel calibration), at room temperature and in a bath of liquid nitrogen respectively, are presented to the interferometer input using an easily accessible laboratory antenna which can be selected as input to the interferometer, instead of the in-vessel antenna normally used during operation. Local calibrations of this kind are performed after every in-vessel calibration providing a reference to which following local calibrations can be compared to evaluate the evolution of the properties of the diagnostic back-end. This procedure only leaves out possible changes related to the waveguides connecting the diagnostic laboratory to the vessel and to the antenna itself. During the D-T campaign period (Autumn-Winter 2021), local calibrations have been performed weekly in order to ensure stability of the calibration. The second technique used to monitor the ECE calibration over long period of time where in-vessel calibrations are not feasible is the so-called B-field ramp calibration[28]. B-field scans in very stable pulses allow to monitor eventual frequency dependent distortions of the ECE spectrum, allowing the correction of the calibration factors set. Pulses of this kind are regularly produced during the commissioning days preceding every JET campaign. The calibration procedures for LIDAR are described in detail in[24,25]. Concerning the temperature measurements in particular, the spectral channels are calibrated independently using a white light source. This is regularly repeated before each experimental campaign. Transmission losses between plasma and spectrometer are instead measured using an in-vessel light source. Further evidence of the stability of LIDAR calibration comes from regular comparison of LIDAR and HRTS data. The two diagnostics are based on similar physical principle but are fully independent instruments whose calibration is measured using different tools and methods. Despite this, they produce very similar T_e measurements over the whole temperature range they cover. It is extremely unlikely that they should be affected by identical systematic errors.

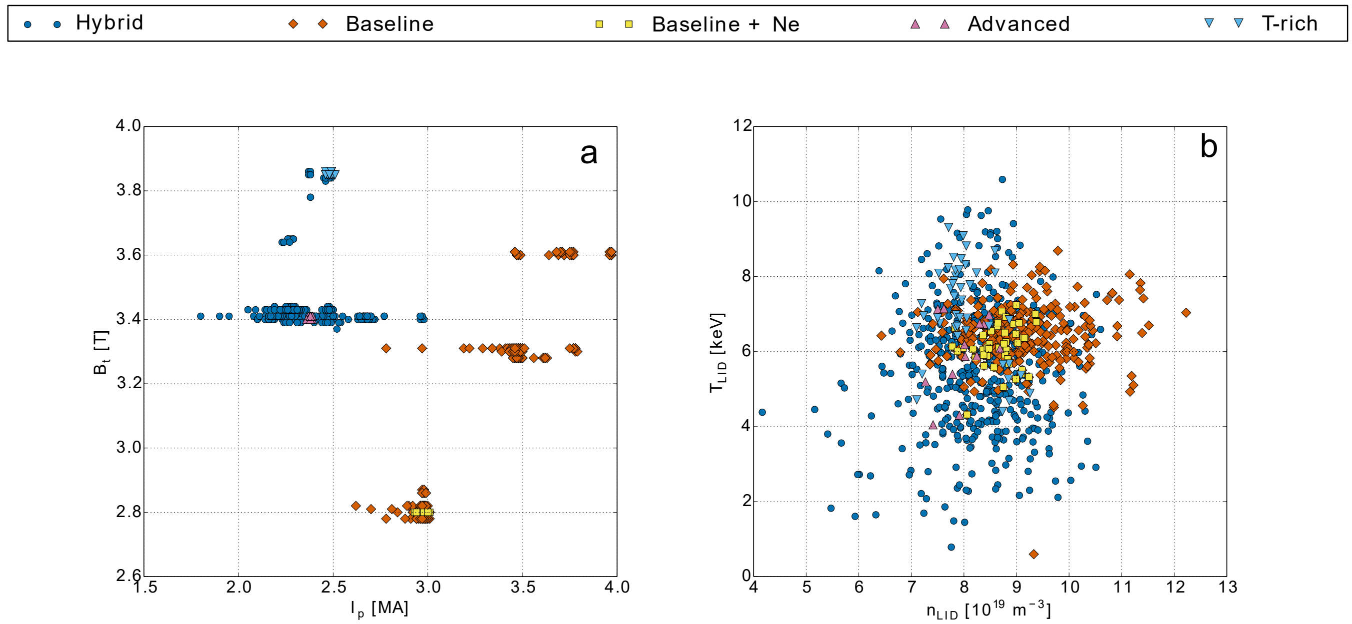

FIG. 2: a): I_p (plasma current) and B_t (toroidal field). b): electron core density n_{LID} and temperature T_{LID} during flat-top phases for pulses in the database.

B. Pulse selection for the database

The database considered here includes experiments carried out from 2019 to 2022, including high performance regimes both in D and in D-T[19]. The high performance baseline scenario focuses on plasmas at low q_{95} ((the safety factor at 95% of the poloidal flux), with $3<q_{95}<3.3$, typically obtained at high plasma current I_p (3-4 MA in the database analyzed) with B_t=2.8-3.5 T. Operation at low gas fuelling in JET-ILW (JET with ITER-like wall) is known to be beneficial to achieve high H-mode performance, but this typically results in low ELM frequency which is challenging for tungsten impurity control and access to stationary conditions. The baseline scenario was first prepared in D, using low gas fuelling and high frequency pellet injection for ELM control which led to high performance H-mode plasmas with stationary conditions in terms of density and radiation[29,30]. The objective was to obtain similarity to the baseline ITER scenario, with $H_{98} \sim 1$ and $\beta_N \sim 1.8$ (β_N=1.5-2.2 in the database analysed), where the normalised β is defined as $\beta_N = \frac{\langle P \rangle}{B_t^2/2\mu_0}\frac{aB_t}{I_p}$ where P is the plasma pressure, a the minor radius and μ_0 is the magnetic permeability of vacuum). Some D pulses in this category used small injections of neon (Ne)[31] in order to control radiation at the plasma edge and thus improving confinement.

High performance discharges of the hybrid type were obtained operating at higher q_{95} ($\sim$4.5 in the database used here) and lower I_p (2.1-3 MA, with B_t=2.8-3.9 T) than in the baseline scenario, aiming at $\beta_N \sim$2.5-3[32,33]. During the D-T campaign, plasmas with a high T content were heated using only Deuterium neutral beams, in order to maximise fusion power produced by the non-thermal plasma components[20]. Other experiments, studying ITB (internal transport barriers) regimes, as well as specific discharges developed to study energetic particles, are also included in the database[34].

Restricting the analysis only to pulses where $T_{e,max} > 5$ keV (246 pulses), all LIDAR times were selected for which T_e>1 keV in the plasma core. For these data entries, the ECE measurements at a time as close as possible to the LIDAR one (less than 10 ms difference), was selected, for a total of more than 3100 comparisons of ECE and LIDAR. Magnetic measurements only have been used for equilibrium reconstruction, in order to determine the ECE temperature profiles. For both ECE and LIDAR, the central temperatures have then been determined averaging the profiles between 2.85 m and 3.15 m. Because of this averaging, small lines of sight differences and uncertainties on the magnetic axis location are smoothed out. The 2nd and 3rd harmonic central temperatures T_{X2} and T_{X3} are instead obtained averaging the ECE spectra in the interval +/- 5% around the frequencies corresponding to the peak for the two harmonics, respectively.

Uncertainties for the ECE measurements are calculated by combining the estimated errors of the calibration procedure and the experimental measurements (see Section 4.F.2 of[26]). A description of the calculation of statistical error calculation for LIDAR can be found in[35].

The database entries correspond to the full discharge evolution (ramp-up, flat-top and ramp-down), excluding times just before disruptions. The combinations of B_t, I_p and n_e, T_e covered by the different scenarios, during the flat top phases, are shown in figures 2a and 2b respectively. Both NBI ($P_{NBI} < 33MW$) and/or ICRH ($P_{ICRH} < 7MW$) heating were used in these discharges, for a maximum power of 38.5 MW ($P_{NBI} = 31.7MW$ and $P_{ICRH} < 6.7MW$), in some of the hybrid pulses.

III. STUDY OF ECE-TS DISCREPANCIES IN THE JET DATABASE

Using the method and averaging described in paragraph II B, a comparison of T_{ECE} and T_{LID} has been carried out, for D and D-T discharges, separately. For D plasmas, on the left side of figure 3, T_{ECE} and T_{LID} have close values for most discharges. However, different scenarios have different behaviours. For instance, baseline discharges with Ne injection, are characterised by $T_{ECE} > T_{LID}$, as in past observations reported for JET and TFTR[3,5,36]. This behaviour is different from that of baseline pulses with no Ne seeding, and with those of the hybrid scenarios. An analogous behaviour is observed for D-T discharges on the right side of figure 3b. Here the largest discrepancies ($T_{LID} > T_{ECE}$) are found for hybrid discharges, in particular for those of the T-rich category, whereas for baseline discharges T_{LID} and T_{ECE} are closer.

Discrepancies are also observed between the core temperatures calculated using the X2 and X3 regions of the ECE spectrum. In both sides of figure 4, for low T_e ($\leq$4 keV), T_{X3} is consistently lower compared with T_{X2} owing to the low values of the optical depth τ_{X3} at low temperature. For higher temperature τ_{X3} increases and, in a Maxwellian plasma, T_{X3} is expected to approach T_{X2}. However, the left side of figure 4, containing D pulses from the database, shows that only a subset of the data has this behaviour whereas, for the majority of the pulses, T_{X3} remains systematically below T_{X2} even when the X3 optical depth is sufficiently high and the plasma is a black body at both harmonics. The same is observed for the D-T discharges, as shown on the right side of figure 4. Interestingly, the behaviour of the various scenarios remains globally different. For example, it is found that the T-rich discharges at high T_e are characterised by close agreement between T_{X2} and T_{X3}, while the hybrid and baseline pulses show $T_{X2} > T_{X3}$. The reduced scattering in each scenario in the D-T pulses, compared with the D sets, is related to the fact that the pulse settings for each scenario had already been optimized during the previous D and T campaigns and experimentation was carried out with little scenario variety, to minimise the use of T and, consequently, the neutron production.

The scenarios considered in this paper cover a large range of density levels and, in some cases, can differ quite substantially from one another (see figures 2a and 2b). Since it is in principle possible that density variations might be playing a role in the observed differences between ECE and LIDAR, figure 5 presents histograms of the ratio T_{LID}/T_{ECE} as a function of the central density value measured by LIDAR (n_{LID}). All histograms are normalised for every density bin and the plot includes all database points shown previously in figures 3 and 4, including all scenarios together. From this, it looks like the discrepancies between ECE and LIDAR are not concentrated at any particular density level, excluding a direct effect of n_e.

Another possible contribution to the explanation for the discrepancy between ECE and LIDAR core measurements could be attributed to the two different lines of sight, as shown in figure 1. Thus, plasmas with the magnetic axis in different positions might cause ECE and LIDAR to view the core more or less directly, causing discrepancies similar to those discussed here. To partially mitigate this effect, T_{LID} and T_{ECE} used in the comparison in figure 3 have been obtained averaging the LIDAR and ECE temperature profiles over a 30 cm range. As is shown in figure 6, the ratio T_{LID}/T_{ECE} between LIDAR and ECE measurements does not seem to be related to the vertical magnetic axis position(z_{axis}). For each scenario, in fact, we can observe the whole range of T_{LID}/T_{ECE} as the plasma axis position changes. Furthermore, the discrepancies observed between 2$^{\text{nd}}$ and 3$^{\text{rd}}$ harmonic peaks for optically thick plasmas, reported in figure 4, are independent from the plasma position since they are acquired using the same diagnostic.

Finally, The observation of differences between the ECE and LIDAR could also be related to the presence of calibration errors arising, for example, from drifts in instrument properties. In the time during which these campaigns occurred in-vessel calibrations were not possible, but the behaviour of the ECE interferometer back-end was continuously monitored with local calibrations and B-field ramps, as described in section II A 1. During the D-T campaign, in particular, local calibrations have been performed weekly. The quality of the calibration could also be generally monitored by the good agreement observed in ohmic phases or, in general, in lower T_e plasmas not just with LIDAR but also with HRTS which is, as already discussed, a completely independent diagnostic. Figure 7 shows histograms for the distribution of the ratio T_{LID}/T_{ECE} as a function of the magnetic field for all the points in the database, over the B range of the scenarios of interest. No systematic deviations can be observed.

IV. MODEL FOR A BIPOLAR DISTORTION OF THE EEDF AND ITS EFFECTS ON ECE AND TS MEASUREMENTS

In order to understand the observed discrepancies and attempt to connect them to distortions of the EEDF, a model for a bipolar perturbation $f_1(p)$ of the distribution function of the electrons $f(p)$ was introduced. Here p is the electron momentum modulus and the unperturbed distribution function is the Maxwellian:

$$f_M = Ae^{-\mu(\gamma-1)},$$

where A is a normalization coefficient, μ the ratio of the electron rest energy and the electron temperature and γ the relativistic factor. The distribution function including the perturbation may then be defined as:

$$f = A(e^{-\mu(\gamma-1)} + f_1). \tag{1}$$

A model perturbation characterized by bipolarity and isotropical structure is then introduced:

$$f_{1u} = f_0 \sin\left[\frac{\pi}{\delta}(p - p_0)\right], \tag{2}$$

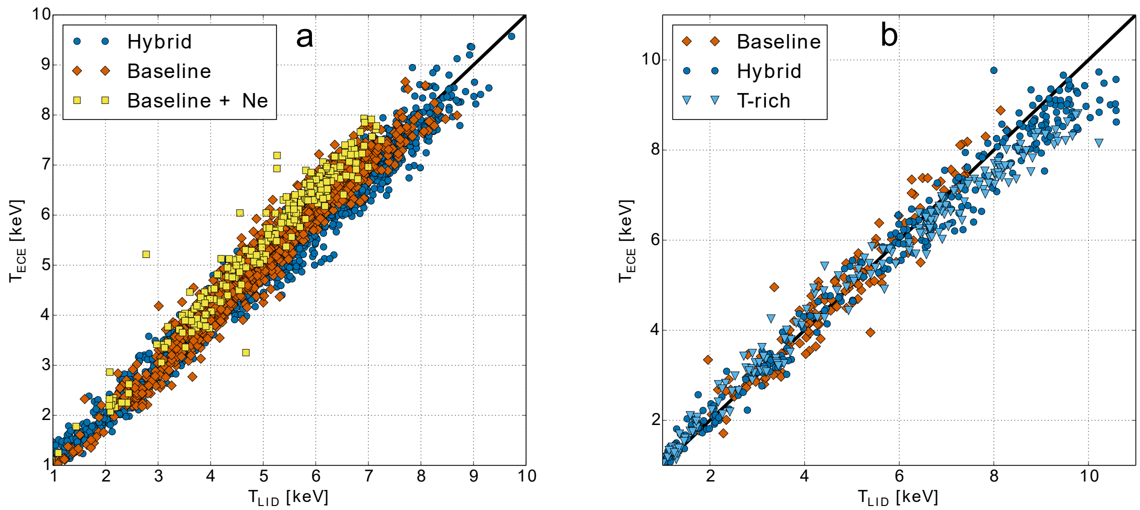

FIG. 3: Comparison of central ECE and LIDAR temperatures in D (a) and D-T (b) pulses.

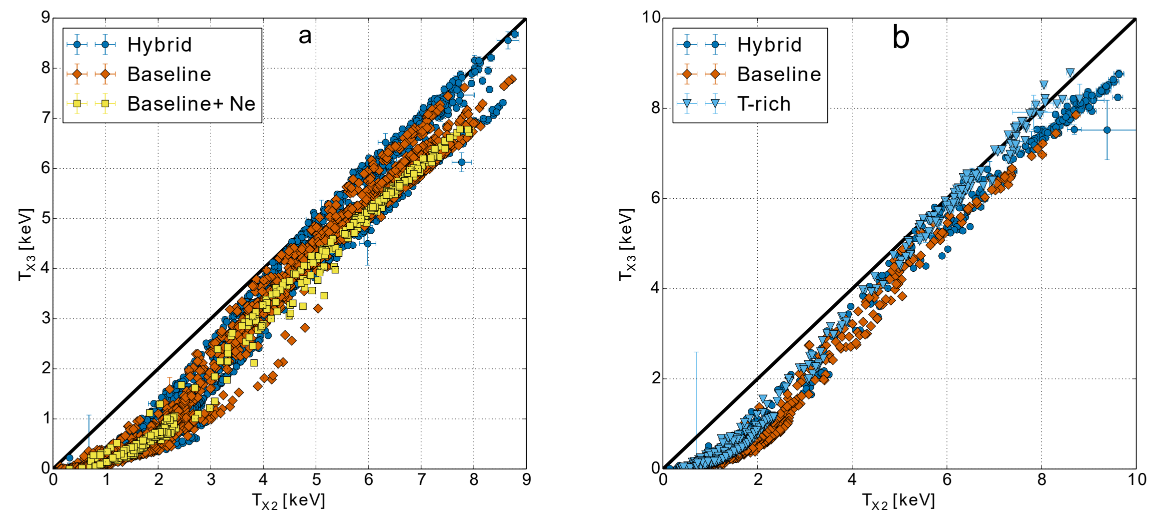

FIG. 4: Central T_e measured by X2 and X3 in D (a) and D-T (b) plasmas.

with $p_0 - \delta < p < p_0 + \delta$. The perturbation is expressed as a function of the amplitude (f_0), and its localisation and extension in momentum space (p_0 and δ respectively). Two plots in figure 8 show this perturbed distribution, where both the localization and the amplitude of the perturbation are varied.

Figure 9 shows the structure of this distribution in the parallel-perpendicular momentum space. Examples of anisotropic distributions are presented in A. In the following only isotropic perturbations will be considered.

With this class of distribution functions, the EC absorption (α) and emission (β) coefficients for waves propagating perpendicularly to the magnetic field can be evaluated analytically. In general, these coefficients are well-known integrals in momentum space (see, for instance, Ref.[14]). An example of these formulas, derived from equations (10)-(13) of[14], for X-mode and n>1, is reported in A. From α and β, the so-called radiation temperature for frequency ω is given by:

$$T_{rad}(\omega) = \int_{R_0-a}^{R_0+a} \beta(R) \exp\left(-\int_{R}^{R_0+a} \alpha(R')dR'\right) dR \quad (3)$$

R being the coordinate along the major radius and a, R_0 are the tokamak radii (minor and major respectively). In equation 3, it is assumed that the receiving antenna is on the low-field side in the torus mid-plane (approximately what happens in the JET geometry).

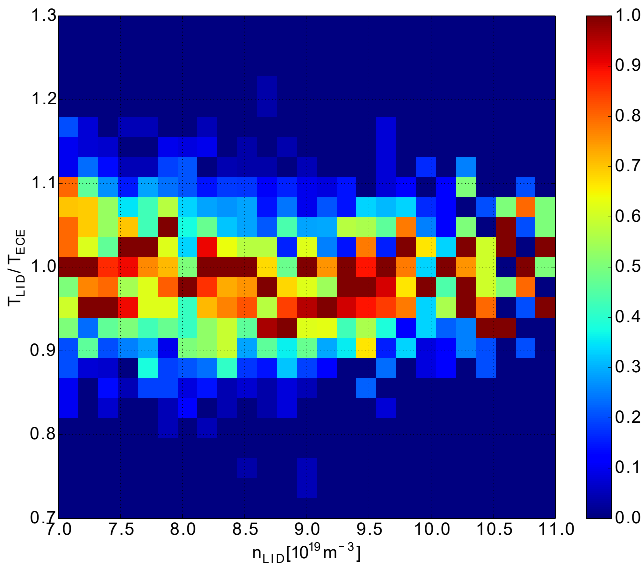

FIG. 5: Histograms of the ratio between LIDAR and ECE core measurements against central density n_{LID} for all pulses. Histograms are normalised for every bin.

Examples of α and β for X2 for a set of frequencies and parameters of the JET tokamak are shown in figure 10 together with the corresponding radiation function:

$$F_{rad} = \beta(R)\exp\left(-\int_{R}^{R_0+a}\alpha(R')dR'\right), \qquad (4)$$

Despite the fact that α and β vs R have a large width, emission localisation is achieved because of the exponential reabsorption multiplicator of β in equation (4).

The ECE resonance condition for an electron in R at the n^{th} harmonic with momentum p is:

$$\omega = \frac{n\omega_c(R)}{\gamma(p)}$$

where $\omega_c(R) = eB(R)/m_e$ is the cold fundamental electron cyclotron resonance at R. This implies that, for a given angular frequency ω, the localisation in electron kinetic energy corresponds to a localisation in the radial profile: $E = m_ec^2(\gamma-1) = m_ec^2(R_c/R-1)$, where R_c is the cold resonance location for $\omega = n\omega_c(R_c)$. F_{rad} (see equation (4)) peaks at a different normalised momentum p/p_{th} (where $p_{th} = m_ev_{th} = (m_eT_e)^{1/2}$) depending on the wave mode, magnetic field gradient, density, electron temperature and the harmonic considered. The temperature dependence is shown in figure 11, where the maxima and the widths of F_{rad} are plotted vs T_e. This figure shows that the radiation measured at different harmonics corresponds to different ranges of the distribution function, because of the dependence of maxima and widths on T_e. This demonstrates that emission at the 2^{nd} and 3^{rd} harmonic ranges is an effective constraint of the EEDF in the range $p_{th} < p < 2p_{th}$, in particular at high temperatures.

In figure 8, the ranges in normalized momentum to which the 2^{nd} and 3^{rd} harmonics are sensitive, for $T_e = 7$ keV, are shown on top of the perturbed EEDFs. Figure 8 clearly shows how the two harmonic domains look at regions of the EEDF that can be differently affected by distortions in different momentum ranges, which, in the model used, is represented by different values of the p_0 parameter. Furthermore, because of the overall temperature dependence, as shown in figure 11, the same perturbation will affect the EC emission more or less significantly, depending on the temperature.

The perturbation, in fact, affects in particular the absorption coefficient, which depends on the derivative of the EEDF ($\alpha \propto \partial f/\partial p_\perp$), as shown in[14]: in general, due to the dependence of F_{rad} on α (see equation (4)), the radiation temperature increases with decreasing absolute value of $\partial f/\partial p_\perp$ for the resonant harmonic range. An example of this is shown in the bottom part of figure 12, where the T_{rad} profiles estimated from the X2 spectrum are computed for $T_{e0} = 3$ and $T_{e0} = 10$ keV. For the same normalized perturbation parameters ($f_0 = 0.03$, $p_0/p_{th} = 1$, $\delta/p_{th} = 0.25$), T_{rad} is significantly enhanced for high T_{e0}, but not affected at low T_{e0}, similar to observations at TFTR and JET[3,5,36]. If the same parameters are used in the computation of Thomson scattering, the effect would be negligible, because the scattered power is just proportional to the distribution function (see, e.g.,[5] and equations (5.8) and (5.9) in[37]). This is illustrated in the top panels of figure 12, where the ECE radiation function and the quantity that plays the same role for Thomson scattering, i.e. the power scattered by a small plasma volume, are plotted versus the kinetic energy normalized to the electron temperature. Clearly, the impact is completely different. This comparison illustrates why the two T_e measurements can be different for non-Maxwellian distributions.

V. COMPARISON OF DATA WITH PREDICTIONS OF THE PERTURBATION MODEL

The model introduced in section IV can now be used to predict the radiation temperature spectrum for the pulses included in the database discussed in section II B, assuming the EEDF in the core was modified by a bipolar distortion. The predicted spectrum is then averaged around the peaks corresponding to the 2^{nd} and 3^{rd} harmonic domains to obtain quantities equivalent to T_{X2} and T_{X3} as described in section II B. In order to calculate these quantities for any given time point, LIDAR temperature and density measurements (T_{LID}, n_{LID}, see figure 2a), and the magnetic field obtained by the equilibrium reconstruction, are used as inputs. For each scenario and isotopic composition, the model parameters (f_0, p_0/p_{th}, δ/p_{th}) that result in good agreement between the prediction and the data are estimated.

In figures 13, 14 and 15, the experimental measurements discussed in section III (T_{X2}, T_{X3}) are compared with the corresponding quantities calculated using the model. In the left side panels (a), the averaged X2 and X3 peak temperatures (predictions and measurements) are plotted against T_{LID}. In the right side panels (b), instead, T_{X3} and the equivalent radiation temperature predicted by the model are directly plotted against the corresponding X2 values. The set of parameters

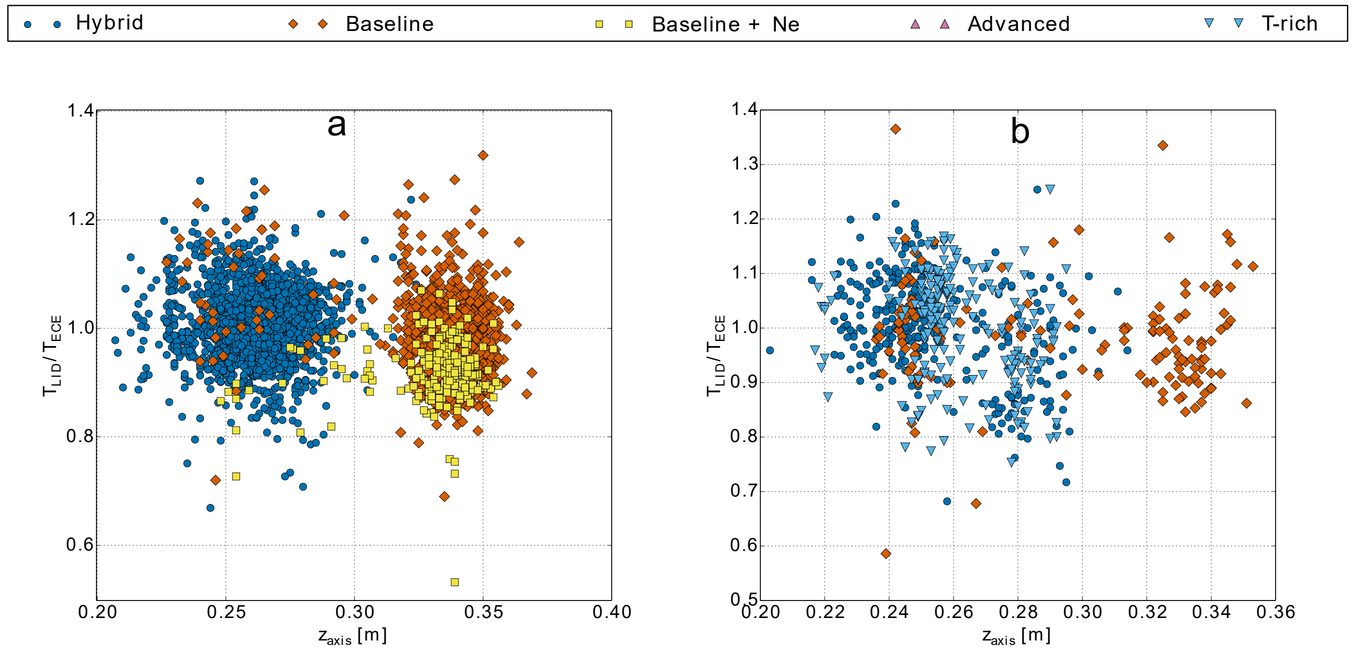

FIG. 6: Ratio between LIDAR and ECE core measurements against the vertical position of the magnetic axis z_{axis} as calculated by the equilibrium reconstruction EFIT for pulses in D (*a*) and D-T (*b*).

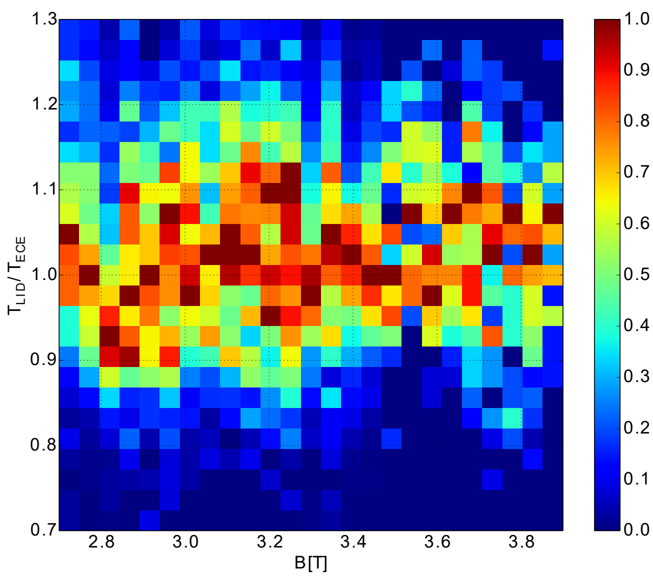

FIG. 7: Histograms of the ratio between LIDAR and ECE core measurements against magnetic field B for all pulses in the database. Histograms are normalised for every bin.

used for the model in the various subsets is displayed at the top of the figures. Error bars for the experimental measurements are shown only in figure 13. The following three series of discharges (discussed in section II B) are considered:

- Figure 13: D pulses with Neon seeding and pellets, with good energy confinement and small ELMs[31].
- Figure 14: D-T pulses in the baseline scenario with low gas fuelling and D pellets.
- Figure 15: D-T hybrid regime pulses.

Figures 13, 14 and 15 all show that the prediction reproduce well the measurements in each scenario with just a <5% distortion of the EEDF, centred at different values and with different widths in normalised momentum. Good agreement between predictions and T_{X3} is found also when τ_{X3} is low ($T_e < 4$ keV). In the D baseline case (figure 13), T_{X3} is found to be closer to LIDAR data than T_{X2} which is instead substantially higher, implying a distortion mainly in the thermal domain (as in the figure 8a). Accordingly, good agreement between model prediction and data is found for $[p_0/p_{th}, \delta/p_{th}] = [1.1, 0.5]$. A similar perturbation could explain similar observations in past JET experiments[5]. When looking at the hybrid D-T discharges in figure 15, instead, T_{X2} tends to be comparable with T_{LID}, suggesting a distortion centred at higher energies. Indeed, for this case, good agreement is reached with $[p_0/p_{th}, \delta/p_{th}]$ = [1.4, 0.8].

In the database, there are cases for which the 3rd but not the 2nd harmonic domains are affected. This is generally found to happen in pulses for which at some time the only heating is ICRH. As a particular illustration, a comparison of model predictions and data was performed for the JET discharge 96850, in a low density ($n_{LID} < 5 \times 10^{19}$ m^{-3}) and high T_e phase. Figure 16 displays good agreement using $[p_0/p_{th}, \delta/p_{th}] = [2, 1]$. In general, ICRH is found to perturb the distribution function at somewhat higher velocities than NBI. For D- T baseline and hybrid discharges, time phases in which only NBI or only ICRH were used have been analyzed (see

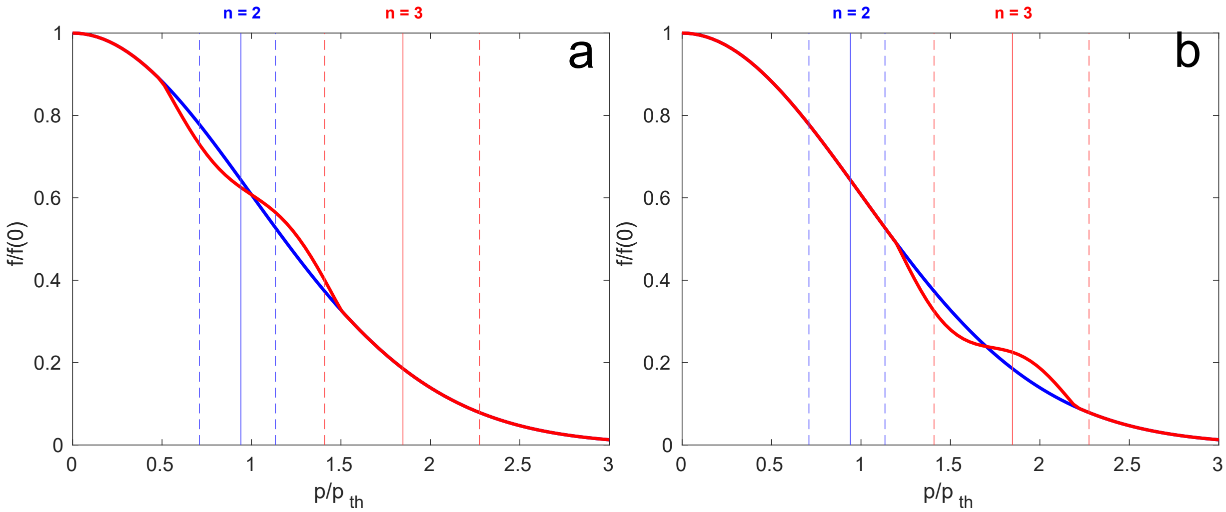

FIG. 8: Normalized one dimensional Maxwellian electron momentum (p) distribution function (blue) and bipolar distortion (red). The domains probed by the 2nd and 3rd harmonic domains for T_e = 7 keV. are indicated by the vertical lines. Perturbations with different locations may affect mainly the 2nd (a) or the 3rd (b) harmonic domain.

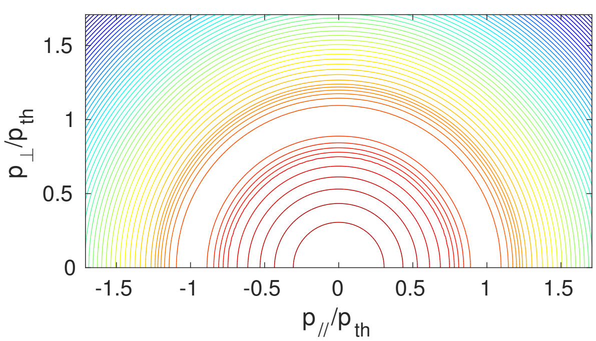

FIG. 9: Level curve representation of a distribution function with a bipolar isotropic perturbation, versus parallel and perpendicular momenta.

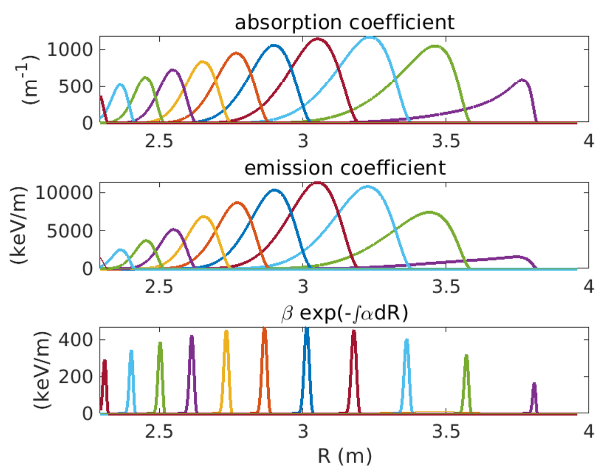

FIG. 10: Electron cyclotron absorption and emission coefficients and radiation function $\beta \exp(-\int \alpha dR)$ for X2 assuming a Maxwellian plasma at $T_e = 10$ keV and JET parameters.

figures 17 and 18). Good agreement with data is reached using $[p_0/p_{th}, \delta/p_{th}] = [1.35, 0.6]$ and $[p_0/p_{th}, \delta/p_{th}] = [1.7, 0.7]$ for NBI only and ICRH only points respectively. In the latter case, also a stronger perturbation was used ($f_0 = 0.05$ versus $f_0 = 0.03$). These findings could be interpreted as a consequence of the different heating mechanisms of NBI and ICRH. The two heating methods, in fact, generate ion tails with distinct characteristics, but they also have different direct effects on electrons. ICRH in particular is expected to have a larger effect on electrons, qualitatively justifying the choice of parameters used here. An in-depth study of the energy transfer between ions and electrons using transport models is outside of the scope of this paper.

The above results indicate that the position where the perturbation is localized in velocity is the most important parameter of the perturbation model. Trends of this parameter with respect to various plasma quantities may give indications on the nature of the non-Maxwellian distortion of the distribution function. Indeed, figure 19 illustrates a smooth and regular dependence of the estimated p_0/p_{th} on various parameters, directly measured or inferred from calculations.

VI. CONCLUSIONS AND PROSPECTS

In this paper, a model for a bipolar distortion of the Maxwellian EEDF was used to investigate the ECE and Thomson scattering discrepancies observed in Te measurements for JET plasmas[5,13]. The model was applied to an extensive database of high-performance plasmas to qualitatively

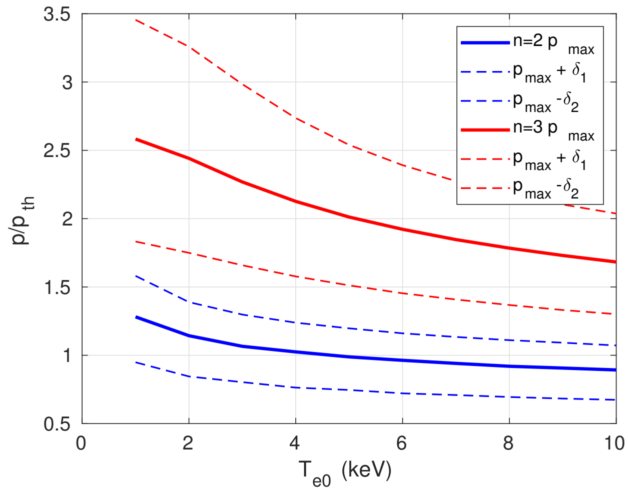

FIG. 11: Momentum normalised to thermal momentum at the maximum of $F_{rad} = \beta \exp(-\int \alpha dR)$ (solid lines) for 2^{nd} (blue) and the 3^{rd} (red) harmonic domains. To either side of the maximum of the radiation function, the dashed likes mark the width at half maximum.

evaluate the agreement with the experimental measurements.

The database includes 246 discharges from high performance D and D-T pulses performed at JET between 2019 and 2022. The T_e data were collected from more than 3100 time points, taken from different phases of the discharge, thus covering a wide range of T_e values. The database includes a variety of plasma scenarios, in some cases not yet tested previously with D-T mixture. Discrepancies were observed bewteen T_e measured by the optically thick 2^{nd} harmonic of the ECE spectrum collected by an interferometer looking mainly at X-mode and T_e measured by a LIDAR system, when high T_e (T_e>5 keV) was reached. Differently from previous results obtained in analogous studies[3–5],in this set of pulses discrepancies are of a smaller size and, remarkably, both cases with $T_{ECE} > T_{LID}$ and cases with $T_{ECE} < T_{LID}$ are found, with different scenarios showing different behaviours. X2 and X3 emission spectra have been compared, finding $T_{X2} > T_{X3}$ in many pulses, also for cases with high τ_{X3} where, for a Maxwellian distribution, $T_{X2} \sim T_{X3}$ was expected.

The comparison between the temperature profiles calculated using the model and the experimental measurements shows that bipolar perturbations of just a few percent, localised between 1-2 times the electrons thermal velocity are sufficient to reproduce the levels of discrepancy observed in the experiments. The effects of the model perturbations on the final temperature profiles are also found to become stronger for higher T_e. This is due to the narrowing of the radiation function (and correspondingly of the width of the emission layer) and to the shifting of its peak to lower momenta. This too is in agreement with the experiments, where the discrepancies between ECE and TS only appeared at high T_e. Indeed, the perturbations only affect ECE profiles, while the different sensitivity to the different regions of momentum space of TS diagnostics make them insensitive to such perturbations. These results suggest that, for conditions where the plasma is optically thick for both 2^{nd} and 3^{rd} X-mode ECE harmonics, measuring them at the same time provides a strong constraint on the EEDF in different parts of the momentum space. This argument could also be expanded to other modes and harmonics that are optically thick.

At this point, it is natural to wonder whether this type of perturbations could significantly affect the ECE temperature diagnostic for ITER plasmas. Assuming that a similar EEDF distortion is present in ITER (which is, of course, only a guess), the model can be used to quantitatively evaluate the impact on the ECE spectra. This is illustrated by the simple case shown in figure 20. Two perturbations with amplitudes that fit JET measurements, same width and located at two different momenta are considered: $p_0/p_{th} = 0.9$ and $p_0/p_{th} = 1.3$. The impact on the temperature profile measured using the O-mode at the 1^{st} harmonic (X2 mode in ITER is likely to suffer from strong reabsorption by the 3^{rd} harmonic resonance[38]) is displayed in the first panel (red symbols and blue symbols, respectively, for the two different perturbations). The effect in ITER is found to be much stronger, because of the much higher temperature (here 25 keV). Moreover, for the two different values of p_0,the effect is opposite. Since the high temperature region ($T_e > 5$ keV) in which the distortion effects are visible now includes a large part of the profile, both trends of the effects can be present in the same profile: note that for $10 < T_e < 15$ keV the radiation temperature profile for $p_0/p_{th} = 1.3$ is higher than both the assumed temperature profile and the prediction for $p_0/p_{th} = 0.9$, whereas it becomes lower beyond 15 keV. Therefore, these distortions on ITER would not just cause discrepancies of T_{e0}, but deformations of the whole profile.

The model developed in this work has been applied to JET results as a tool for data analysis. It does not provide an interpretation of the cause of the possible EEDF distortions and, currently, only hypotheses can be formulated in this regard. All the JET and TFTR discharges in which this phenomenon has been observed were heated by NBI and/or ICRH and, in the case of D-T, alpha particles and it is well known that these heating sources are characterized by the presence of fast ion tails. These tails could then be a candidate as a source of distortions of the electron distribution. Interaction of energetic ions with the electrons could take place because of:

- relaxation of the energetic ion tail on the electrons by Coulomb collisions;
- MHD modes driven by energetic ions (e.g., Alfvén modes) exchanging their energy with the electrons (e.g., absorption by Landau damping).

It is a common assumption that, despite collisional interaction with fast ions, the EEDF conserve its Maxwellian shape, because the fast ion velocity is much smaller that the electron thermal velocity. However, speaking of small perturbations, the full integro-differential collision operator should be used in the kinetic computation, which is not usually the case. Bipolar distortions of distribution functions in the thermal velocity range are not an uncommon phenomenon in plasmas.

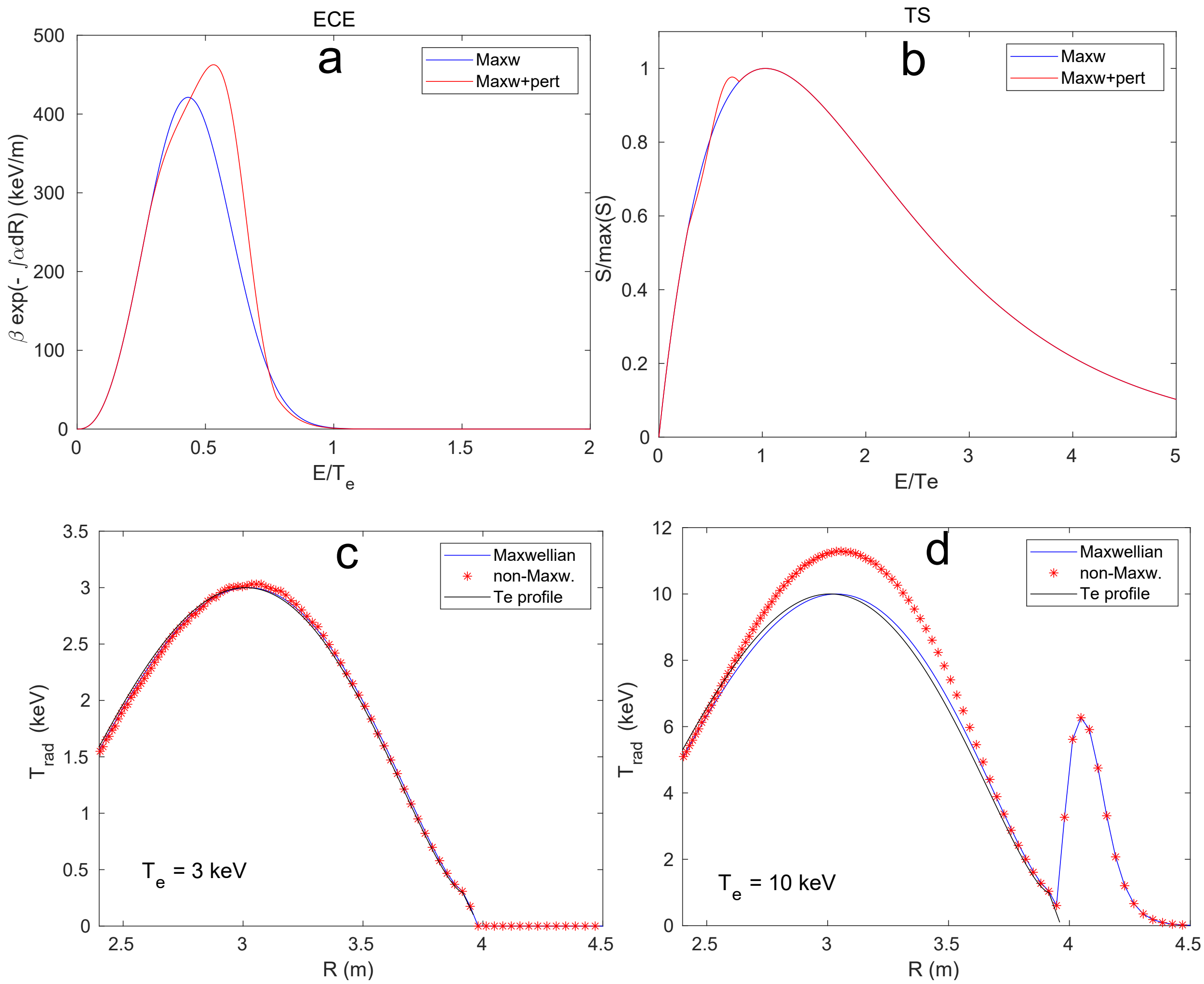

FIG. 12: Top: radiation function for 2nd harmonic X-mode (a) and normalised Thomson scattered power (b) versus ratio of electron kinetic energy and electron temperature. Predictions are made for a pure Maxwellian (blue) and perturbed (red) distribution. Bottom: predicted T_{rad} vs R, for $T_{e0} = 3$ keV (c) and $T_{e0} = 10$ keV (d). Assumed T_e profile (black), and calculations using a Maxwellian (blue) and a perturbed distribution (red asterisks) are shown for each case. Radiation temperature is mapped on the major radius coordinate R considering, for each frequency, the cold resonance position. Parameters of the perturbation model: $f_0 = 0.03$, $p_0/p_{th} = 1$, $\delta/p_{th} = 0.25$.

While the parameters range of the plasmas involved in these cases are obviously very far from those of a tokamak, it is interesting to mention that a bipolar perturbation of the EEDF has been found in kinetic calculations performed for inertial fusion plasmas[15], precisely due to collisional interaction with the ions. Direct observation of bipolar ion distributions due to wave-particle interaction in laboratory plasmas has been recently reported[39]. Concerning the interaction with MHD modes, bipolar perturbations of the EEDF at thermal velocities have been observed in the magnetosheath[16]. Gyrokinetic analysis has led to interpreting these observations as due to kinetic Alfven waves[17], delivering energy to the electrons by means of Landau damping. Of course, phenomena observed in such nearly collisionless plasmas cannot be directly extrapolated to fusion plasmas. Nevertheless, the analogy can be exploited by carrying out gyrokinetic simulations for several MHD modes present in high performance JET plasmas, not necessarily only those driven by energetic ions.

In summary, the experimental results reported and analyzed here lead to the conclusion that Thomson scattering is, by its nature, very weakly sensitive to the detailed shape of the electron distribution. As a consequence, a TS system is generally adequate in order to measure the electron temperature profile. On the other hand, ECE spectra, and the corresponding profiles, may be affected significantly by a small-amplitude perturbation (a few percent) of the EEDF in the range from once or twice the bulk thermal velocities. Hence, ECE temperature measurements should be considered less reliable than those of TS for plasmas relevant to a fusion power plant. However, such a sensitivity to the EEDF shape can be used to obtain

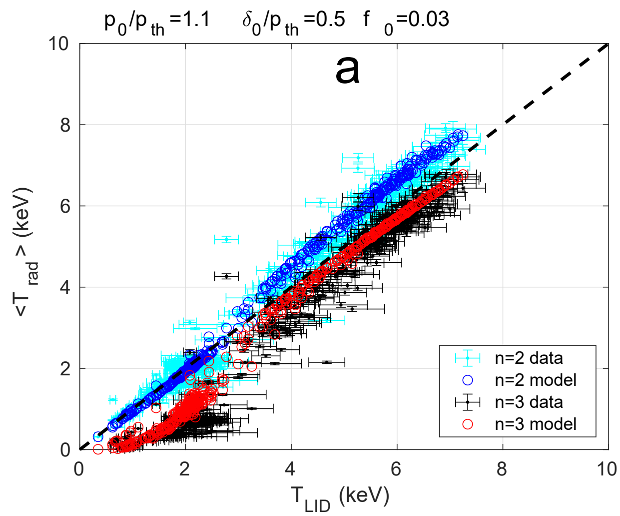

FIG. 13: Measurements (with error bars) of central temperature compared with perturbation model, for a series of JET D pulses with neon seeding and pellets. Parameters of the model: $f_0 = 0.03$, $p_0/p_{th} = 1.1$, $\delta/p_{th} = 0.5$. a): T_{rad} averaged between $\pm 5\%$ of the frequency corresponding to the 2$^{\text{nd}}$ and 3$^{\text{rd}}$ hharmonic maxima versus the corresponding values of T_{LID} in the database; b): 3$^{\text{rd}}$ harmonic versus 2$^{\text{nd}}$ harmonic T_{e0} measurements.

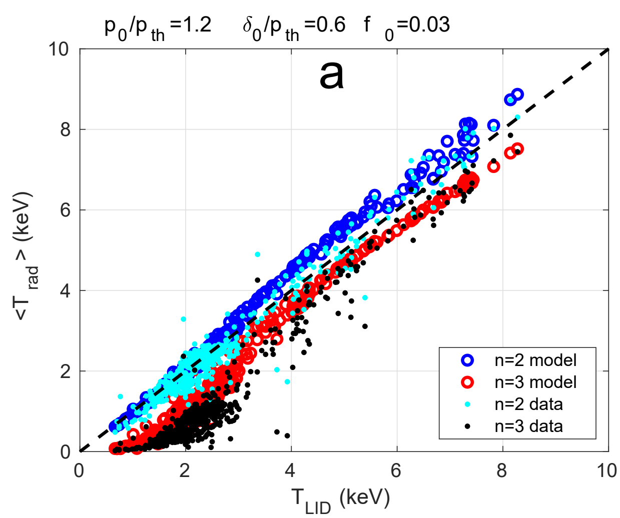

FIG. 14: As in figure 13, for a series of D-T pulses in the baseline regime. Parameters of the model: : $f_0 = 0.03$, $p_0/p_{th} = 1.2$, $\delta/p_{th} = 0.6$.

a constraint on possible perturbations of the electron distribution function, a very useful property for physics studies. TS and ECE systems should thus be understood as complementary measurement techniques, providing redundancy only when probing a Maxwellian plasma. In a machine employing independently calibrated ECE and TS diagnostics, this redundancy will ensure the collection of evidence for the appearance of non-Maxwellian features. An ECE system optimised for this kind of applications should be able to probe ordinary and extra-ordinary wave mode spectra over several harmonic domains, and possibly using lines of sight both perpendicular and oblique with respect to the magnetic field.

Appendix A: Derivation of absorption and emission coefficients for ECE

The absorption and emission coefficients for the extraordinary wave and n>1 can be calculated starting from the perturbed distribution functions described in Section IV, using for example, formulas from equations (10)-(13) of[14]:

$$(\alpha,\beta) = A_0 \Sigma_n (\alpha_n, \beta_n) \tag{A1}$$

with:

$$A_0 = \frac{2\pi^2}{N_X} \frac{\omega}{c} \frac{\omega_p^2}{\omega^2} \left| 1 - \frac{i\varepsilon_{12}}{\varepsilon_{11}} \right|^2 \frac{\mu e^{-\mu}}{4\pi K_2(\mu)}.$$

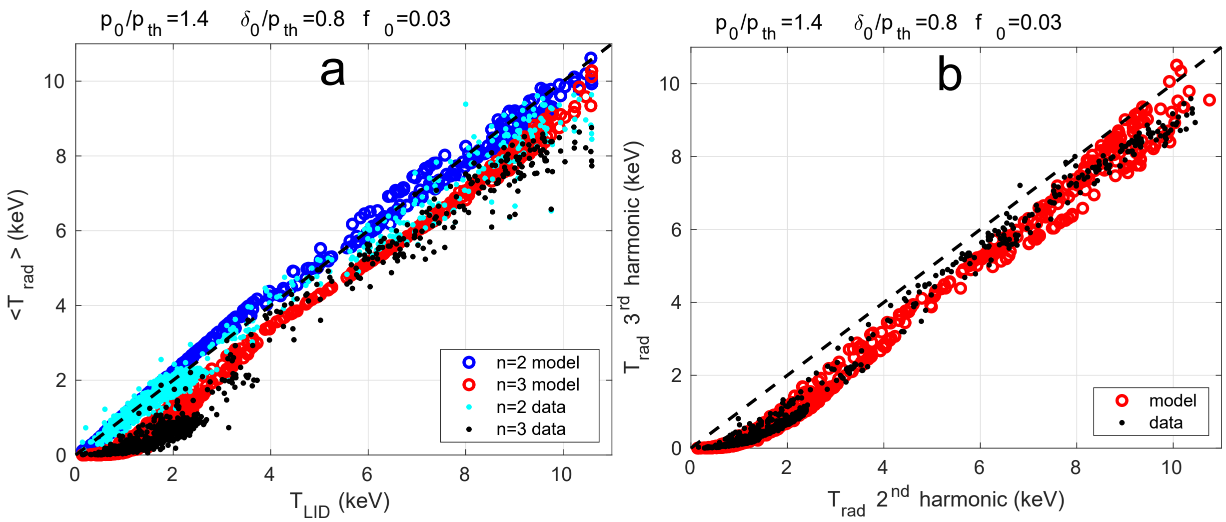

FIG. 15: As in figure 13, for a series of D-T pulses in the hybrid regime. Parameters of the model: $f_0 = 0.03$, $p_0/p_{th} = 1.4$, $\delta/p_{th} = 0.8$.

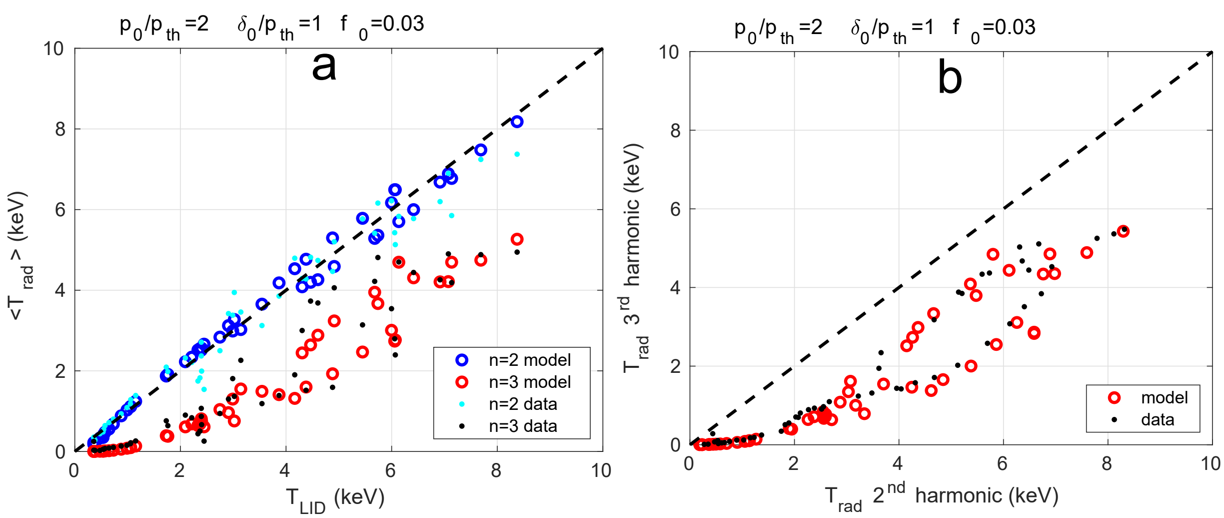

FIG. 16: As in figure 13, for pulse 96850 ($B_t = 3.3$ T, $I_p = 2.4$ MA, $P_{ICRH} = 0-4$ MW, $P_{NBI} = 10-27$ MW). Parameters of the model: $f_0 = 0.03$, $p_0/p_{th} = 2$, $\delta/p_{th} = 1$.

Here n is the harmonic number, ω, ω_p and ω_c are respectively the angular wave frequency, the plasma frequency and the cyclotron frequency, multiplied by 2π. Finally, N_X is the cold refractive index and ε is the cold plasma dielectric tensor.

The nth components of the absorption and emission coefficients are:

$$\alpha_n = A_n \left[\frac{\mu u_n}{n\omega_c/\omega} e^{-\mu\left(\frac{n\omega_c}{\omega}-1\right)} - Q_n h(u_n) \frac{\pi}{\delta/mc} f_0 \cos\left(\frac{\pi}{\delta/mc}(u_n - u_0)\right)\right]$$

$$\beta_n = A_n \frac{mc^2 u_n}{n\omega_c/\omega}\left[e^{-\mu\left(\frac{n\omega_c}{\omega}-1\right)} + Q_n h(u_n) f_0 \sin\left(\frac{\pi}{\delta/mc}(u_n - u_0)\right)\right].$$

In these equations:

$$A_n = \mu^{(n-1)} \frac{n\omega_c}{\omega} u_n^{2n} \left(\frac{N_X \omega}{\sqrt{\mu}\,\omega_c}\right)^{2(n-1)} \frac{B(n+1, 1/2)}{[2^n (n-1)!]^2},$$

$$u_n = \left[\left(\frac{n\omega_c}{\omega}\right)^2 - 1\right]^{1/2},\ u_0 = \frac{p_0}{mc},$$

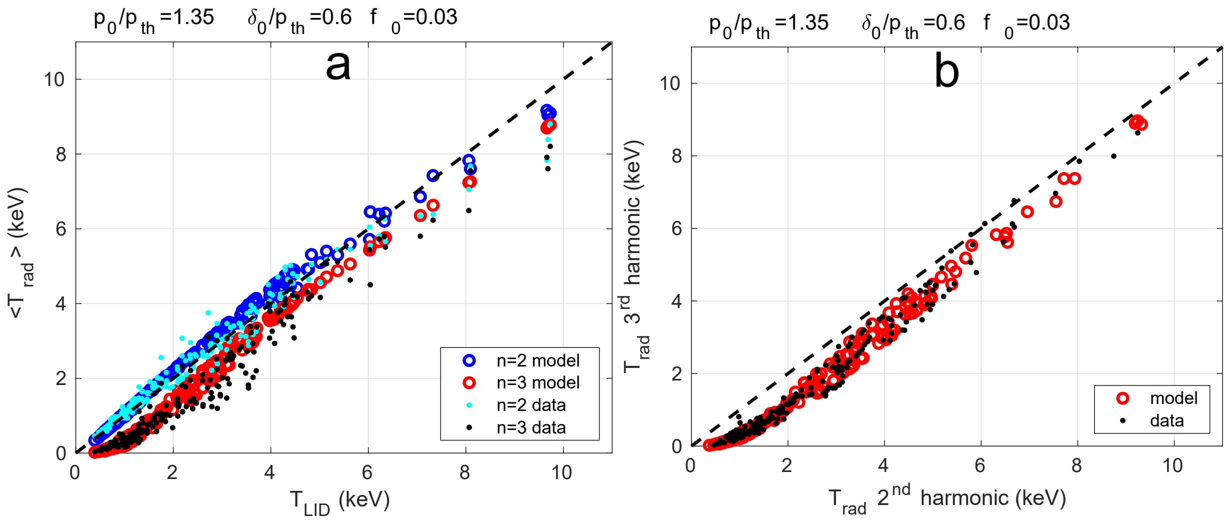

FIG. 17: As in figure 13, for D-T pulses and phases with NBI heating only. Parameters of the model: $f_0 = 0.03$, $p_0/p_{th} = 1.35$, $\delta/p_{th} = 0.6$.

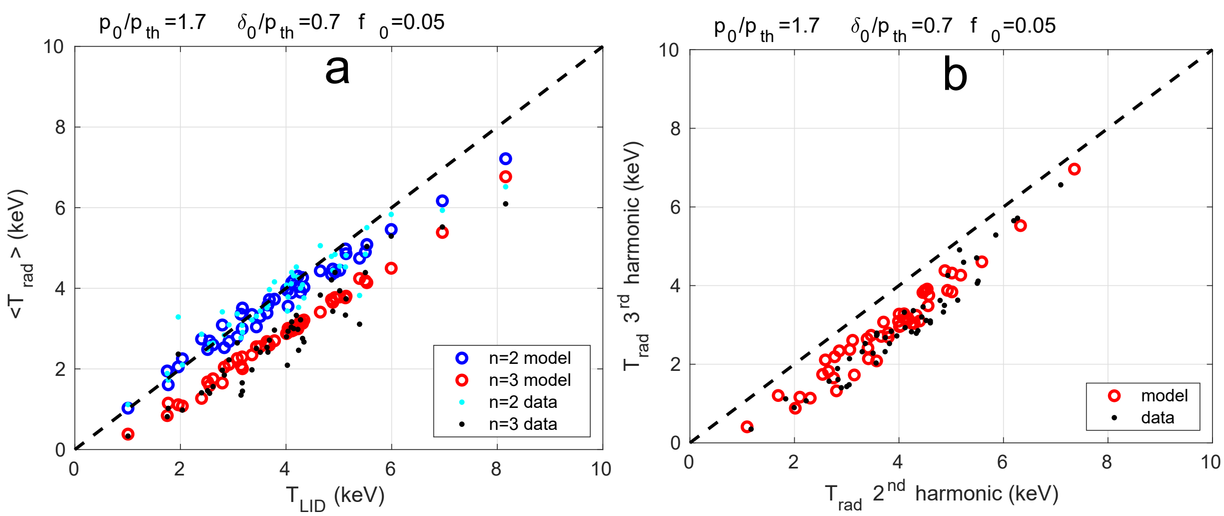

FIG. 18: As in figure 13, for D-T pulses and phases with ICRH only. Parameters of the model: $f_0 = 0.05$, $p_0/p_{th} = 1.7$, $\delta/p_{th} = 0.7$.

$$h(u_n) = H\left(u_n - u_0 + \frac{\delta}{mc}\right) H\left(u_0 + \frac{\delta}{mc} - u_n\right).$$

Here $B(x,y)$ and H are the Beta and the Heaviside functions respectively. The function Q_n is related to the pitch-angle dependence of the distribution function perturbation. For the isotropic perturbation f_{1u} (see equation (2)), $Q_n = 1$. For some examples of anisotropic perturbations

$$f_{1s} = f_{1u}\sin\theta,$$

$$f_{1c} = f_{1u}\cos\theta,$$

$$f_{1s2} = f_{1u}\sin^2(2\theta),$$

$$f_{1c2} = f_{1u}\cos^2\theta,$$

the corresponding Q_n functions are:

$$f_1 = f_{1s} \to Q_n = \frac{B(n+3/2,1/2)}{B(n+1,1/2)},$$

$$f_1 = f_{1c} \to Q_n = \frac{B(n+1,1)}{B(n+1,1/2)},$$

$$f_1 = f_{1s2} \to Q_n = \frac{B(n+2,3/2)}{B(n+1,1/2)},$$

$$f_1 = f_{1c2} \to Q_n = \frac{B(n+1,3/2,1/2)}{B(n+1,1/2)}.$$

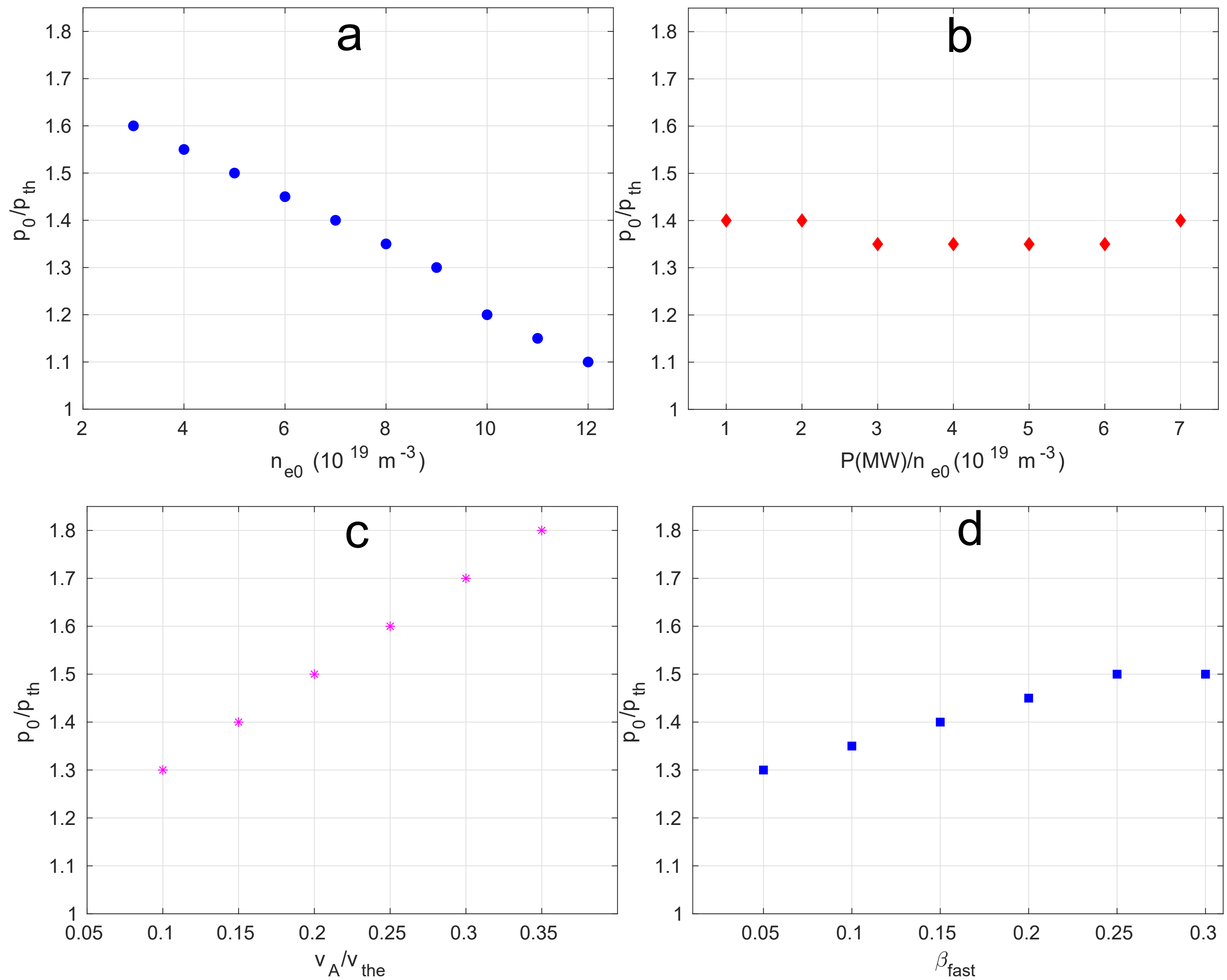

FIG. 19: Position of the perturbation in normalised momentum space providing the best fit of the full set of discharges in the database. Each plot correspond to a selection of values for a given physical quantity. Density at the plasma center (a), heating power divided by the central density (b), ratio of Alfvén velocity and the electron thermal velocity (c) and fast ion pressure normalized to the magnetic pressure (d).

ACKNOWLEDGMENTS

This work has been carried out within the framework of the EUROfusion Consortium, funded by the European Union via the Euratom Research and Training Programme (Grant Agreement No 101052200 — EUROfusion). Views and opinions expressed are however those of the author(s) only and do not necessarily reflect those of the European Union or the European Commission. Neither the European Union nor the European Commission can be held responsible for them.

This work has been part-funded by the EPSRC Energy Programme [grant number EP/W006839/1].

For the purpose of open access, the authors have applied a Creative Commons Attribution (CC BY) licence to any Author Accepted Manuscript version arising.

[1] A. E. Costley, R. J. Hastie, J. W. M. Paul, and J. Chamberlain. Electron Cyclotron Emission from a Tokamak Plasma: Experiment and Theory. *Phys. Rev. Lett.*, 33(13):758–761, September 1974.

[2] John Sheffield. Chapter 9 - Scattering from a High-Temperature Plasma. In John Sheffield, editor, *Plasma Scattering of Electromagnetic Radiation*, pages 191–210. Academic Press, January 1975.

[3] G. Taylor, E. Fredrickson, B. Grek, and A. Janos. Electron Cyclotron Emission Measurements on High \beta TFTR Plasmas. page 485, Borrego Springs, California, January 1995. World Scientific Publishing Co. Pte. Ltd.

[4] I. Fidone, G. Giruzzi, and G. Taylor. Plasma diagnostics in the Tokamak Fusion Test Reactor using emission of electron cyclotron radiation at arbitrary frequencies. *Physics of Plasmas*, 3(6):2331–2336, June 1996.

[5] E. de la Luna, V. Krivenski, G. Giruzzi, C. Gowers, R. Prentice, J. M. Travere, and M. Zerbini. Impact of bulk non-Maxwellian electrons on electron temperature measurements (invited). *Review of Scientific Instruments*, 74(3):1414–1420, March 2003.

[6] E. De La Luna, D. Farina, L. Figini, G. Grosseti, S. Nowak, C. Sozzi, M. Beurskens, O. Ford, T. Johnson, and EFDA contributors Jet. Recent results on the discrepancy between electron temperature measurements in

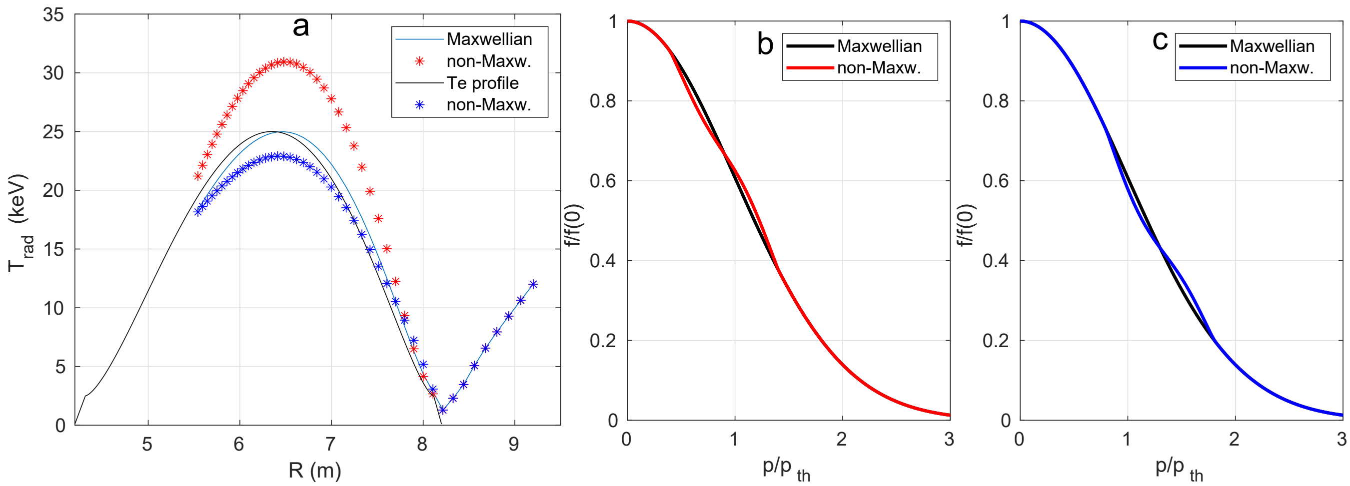

FIG. 20: *a*: ECE temperature profile computed from the 1st harmonic O-mode peak calculated for ITER-like parameters ($T_{e0} = 25$ keV). The figure contains the input T_e profile for the calculations (black), a calculation assuming a Maxwellian distribution (cyan) and two calculations using the model, with model parameters: $f_0 = 0.03$, $\delta/p_{th} = 0.5$, $p_0/p_{th} = 0.9$ (*b*, red) and $p_0/p_{th} = 1.3$ (*c*, blue), respectively.

high temperature plasmas in jet. In *Electron Cyclotron Emission and Electron Cyclotron Resonance Heating (EC-15)*, pages 200–207. WORLD SCIENTIFIC, April 2009.

[7]K. V. Beausang, S. L. Prunty, R. Scannell, M. N. Beurskens, M. J. Walsh, and E. de La Luna. Detecting non-Maxwellian electron velocity distributions at JET by high resolution Thomson scattering. *Review of Scientific Instruments*, 82(3):033514, March 2011. Publisher: American Institute of Physics.

[8]L.-G. Eriksson, T. Hellsten, and U. Willen. Comparison of time dependent simulations with experiments in ion cyclotron heated plasmas. *Nucl. Fusion*, 33(7):1037, July 1993.

[9]A. E. White, A. E. Hubbard, J. W. Hughes, P. T. Bonoli, M. E. Austin, A. Bader, R. W. Harvey, Y. Lin, Y. Ma, M. L. Reinke, S. M. Wolfe, and S. J. Wukitch. Investigation of the Thomson scattering-ECE discrepancy in ICRF heated plasmas at Alcator C-Mod. *Nucl. Fusion*, 52(6):063021, May 2012. Publisher: IOP Publishing.

[10]G. Pucella, E. Alessi, S. Almaviva, B. Angelini, M. L. Apicella, G. Apruzzese, M. Aquilini, G. Artaserse, B. Baiocchi, M. Baruzzo, F. Belli, W. Bin, F. Bombarda, L. Boncagni, S. Briguglio, A. Bruschi, P. Buratti, G. Calabrò, M. Cappelli, A. Cardinali, N. Carlevaro, D. Carnevale, L. Carraro, C. Castaldo, F. Causa, R. Cavazzana, S. Ceccuzzi, P. Cefali, C. Centioli, R. Cesario, S. Cesaroni, C. Cianfarani, M. Ciotti, G. Claps, F. Cordella, F. Crisanti, Y. Damizia, O. D'Arcangelo, M. De Angeli, E. Di Ferdinando, S. Di Giovenale, C. Di Troia, A. Dodaro, B. Esposito, M. Falessi, F. Fanale, D. Farina, L. Figini, G. Fogaccia, D. Frigione, V. Fusco, L. Gabellieri, G. Gallerano, S. Garavaglia, G. Ghillardi, G. Giacomi, E. Giovannozzi, G. Gittini, G. Granucci, G. Grosso, L. A. Grosso, M. Iafrati, L. Laguardia, E. Lazzaro, D. Liuzza, M. Lontano, G. Maddaluno, S. Magagnino, M. Marinucci, D. Marocco, G. Mazzitelli, C. Mazzotta, C. Meineri, V. Mellera, M. Mezzacappa, A. Milovanov, D. Minelli, F. C. Mirizzi, G. Montani, A. Moro, F. Napoli, S. Nowak, F. P. Orsitto, D. Pacella, F. Pallotta, S. Palomba, L. Panaccione, A. Pensa, V. Pericoli-Ridolfini, P. Petrolini, V. Piergotti, C. Piron, A. Pizzuto, S. Podda, M. E. Puiatti, G. Ramogida, B. Raspante, G. Ravera, D. Ricci, N. Rispoli, G. Rocchi, A. Romano, G. Rubino, S. Rueca, M. Scisciò, L. Senni, A. Sibio, A. Simonetto, C. Sozzi, U. Tartari, A. Taschin, B. Tilia, G. Trentuno, A. A. Tuccillo, O. Tudisco, R. Tulli, M. Valisa, M. Vellucci, B. Viola, E. Vitale, G. Vlad, D. Zannetti, B. Zaniol, M. Zerbini, F. Zonca, V. K. Zotta, M. Angelone, C. Barcellona, L. Calacci, L. Caneve, F. Colao, B. Coppi, S. Galeani, C. Galperti, P. Gasior, W. Gromelski, M. Hoppe, M. Kubkowska, V. Lazic, M. Lehnen, M. Marinelli, F. Martinelli, E. Milani, P. Mosetti, P. Muscente, E. Nardon, M. Passeri, A. Reale, M. Sassano, A. Selce, C. Verona, and G. Verona-Rinati. Overview of the FTU results. *Nucl. Fusion*, 62(4):042004, March 2022. Publisher: IOP Publishing.

[11]P. Gomez, J. L. Ségui, and G. Giruzzi. Temporal analysis and simulation of ECE spectra during LHCD in tore supra. *AIP Conference Proceedings*, 485(1):411–414, September 1999. Publisher: American Institute of Physics.

[12]Vladimir Krivenski. Electron cyclotron emission by non-Maxwellian bulk distribution functions. *Fusion Engineering and Design*, 53(1):23–33, January 2001.

[13]V Krivenski. Evidence of Non-Maxwellian Electron Bulk Distributions on JET. *29th EPS Conf. on Plasma Physics, ECA*, 26B, 2002.

[14]G. Giruzzi. Electron cyclotron emission during electron cyclotron heating in tokamaks. *Nucl. Fusion*, 28(8):1413–1425, August 1988. Publisher: IOP Publishing.

[15]B. Appelbe, M. Sherlock, O. El-Amiri, C. Walsh, and J. Chittenden. Modification of classical electron transport due to collisions between electrons and fast ions. *Physics of Plasmas*, 26(10):102704, October 2019. Publisher: American Institute of Physics.

[16]C. H. K. Chen, K. G. Klein, and G. G. Howes. Evidence for electron Landau damping in space plasma turbulence. *Nat Commun*, 10(1):740, February 2019. Number: 1 Publisher: Nature Publishing Group.

[17]Sarah A. Horvath, Gregory G. Howes, and Andrew J. McCubbin. Electron Landau damping of kinetic Alfvén waves in simulated magnetosheath turbulence. *Physics of Plasmas*, 27(10):102901, October 2020. Publisher: American Institute of Physics.

[18]F. Romanelli. Overview of the JET results with the ITER-like wall. *Nucl. Fusion*, 53(10):104002, September 2013. Publisher: IOP Publishing.

[19]J. Mailloux. Deuterium-tritium experiments in JET with the ITER-like wall. In *Fusenet - Indico (Indico)*, June 2022.

[20]M. Maslov, E. Lerche, C. D. Challis, J. Hobirk, A. Kappatou, D. B. King, D. Keeling, F. Rimini, E. De La Luna, I. Monakhov, P. Jacquet, C. F. Maggi, J. Garcia, J. Mailloux, Y. Kazakov, M. Marin, D. Van Eester, G. Pucella, Z. Stancar, D. Rigamonti, J. Eriksson, M. Nocente, G. Matthews, K. Kirov, V. Kiptily, A. Chomiczewska, I. Ivanova-Stanik, F. Auriemma, and R. Lorenzini. T-rich scenario for the record fusion energy plasma in JET DT. In *Bulletin of the American Physical Society*. American Physical Society, October 2022.

[21]R. Pasqualotto, P. Nielsen, C. Gowers, M. Beurskens, M. Kempenaars, T. Carlstrom, and D. Johnson. High resolution Thomson scattering for Joint European Torus (JET). *Review of Scientific Instruments*, 75(10):3891–3893, October 2004.

[22]L. Frassinetti, M. N. A. Beurskens, R. Scannell, T. H. Osborne, J. Flana-

gan, M. Kempenaars, M. Maslov, R. Pasqualotto, and M. Walsh. Spatial resolution of the JET Thomson scattering system. *Review of Scientific Instruments*, 83(1):013506, January 2012.

[23] H. Salzmann and K. Hirsch. Proposal for a time-of-flight Thomson backscattering technique for large fusion devices. *Review of Scientific Instruments*, 55(4):457–462, April 1984. Publisher: American Institute of Physics.

[24] H. Salzmann, J. Bundgaard, A. Gadd, C. Gowers, K. B. Hansen, K. Hirsch, P. Nielsen, K. Reed, C. Schrödter, and K. Weisberg. The LIDAR Thomson scattering diagnostic on JET (invited). *Review of Scientific Instruments*, 59(8):1451–1456, August 1988. Publisher: American Institute of Physics.

[25] M. Maslov, M. N. A. Beurskens, M. Kempenaars, and J. Flanagan. Status of the JET LIDAR Thomson scattering diagnostic. *J. Inst.*, 8(11):C11009–C11009, November 2013. Publisher: IOP Publishing.

[26] S. Schmuck, J. Fessey, J. E. Boom, L. Meneses, P. Abreu, E. Belonohy, and I. Lupelli. Electron cyclotron emission spectra in X- and O-mode polarisation at JET: Martin-Puplett interferometer, absolute calibration, revised uncertainties, inboard/outboard temperature profile, and wall properties. *Review of Scientific Instruments*, 87(9):093506, September 2016.

[27] E. de la Luna, J. Sánchez, V. Tribaldos, EFDA contributors Jet, G. Conway, W. Suttrop, J. Fessey, R. Prentice, C. Gowers, and J. M. Chareau. Electron cyclotron emission radiometer upgrade on the Joint European Torus (JET) tokamak. *Review of Scientific Instruments*, 75(10):3831–3833, October 2004. Publisher: American Institute of Physics.

[28] Patrick Blanchard, Elena de la Luna, and Chris Gowers. Improvement of the Te profile on Joint European Torus measured by electron cyclotron emission. *Review of Scientific Instruments*, 75(10):3828–3830, October 2004. Publisher: American Institute of Physics.

[29] L. Garzotti, C. Challis, R. Dumont, D. Frigione, J. Graves, E. Lerche, J. Mailloux, M. Mantsinen, F. Rimini, F. Casson, A. Czarnecka, J. Eriksson, R. Felton, L. Frassinetti, D. Gallart, J. Garcia, C. Giroud, E. Joffrin, Hyun-Tae Kim, N. Krawczyk, M. Lennholm, P. Lomas, C. Lowry, L. Meneses, I. Nunes, C. M. Roach, M. Romanelli, S. Sharapov, S. Silburn, A. Sips, E. Stefániková, M. Tsalas, D. Valcarcel, and M. Valovič and. Scenario development for D–T operation at JET. *Nucl. Fusion*, 59(7):076037, June 2019. Publisher: IOP Publishing.

[30] J. Garcia, F. J. Casson, C. D. Challis, A. Field, L. Garzotti, H. T. Kim, J. Mailloux, F. Rimini, G. Szepesi, D. Van Eester, E. Lerche, D. Frigione, J. Hobirk, A. Kappatou, S. Mazzi, E. De La Luna, Z. Stancar, M. Poradziński, F. Auriemma, R. Lorenzini, J. Citrin, M. Marin, J. Ferreira, E. Fransson, P. Strand, R. Gatto, and V. K. Zotta. Integrated scenario development at JET for DT operation and ITER risk mitigation. In *IAEA FEC 2021*, Nice, May 2021.

[31] J. Garcia, E. de la Luna, M. Sertoli, F. J. Casson, S. Mazzi, Ž. Štancar, G. Szepesi, D. Frigione, L. Garzotti, F. Rimini, D. van Eester, P. Lomas, C. Sozzi, N. Aiba, M. Dicorato, A. Mariani, R. Coelho, L. Frasinetti, G. T. A. Huijsmans, and F. Liu. New H-mode regimes with small ELMs and high thermal confinement in the Joint European Torus. *Physics of Plasmas*, 29(3):032505, March 2022. Publisher: American Institute of Physics.

[32] J. Hobirk, F. Imbeaux, F. Crisanti, P. Buratti, C. D. Challis, E. Joffrin, B. Alper, Y. Andrew, P. Beaumont, M. Beurskens, A. Boboc, A. Botrugno, M. Brix, G. Calabro\textquotesingle, I. Coffey, S. Conroy, O. Ford, D. Frigione, J. Garcia, C. Giroud, N. C. Hawkes, D. Howell, I. Jenkins, D. Keeling, M. Kempenaars, H. Leggate, P. Lotte, E. de la Luna, G. P. Maddison, P. Mantica, C. Mazzotta, D. C. McDonald, A. Meigs, I. Nunes, E. Rachlew, F. Rimini, M. Schneider, A. C. C. Sips, J. K. Stober, W. Studholme, T. Tala, M. Tsalas, I. Voitsekhovitch, and P. C. de Vries and. Improved confinement in JET hybrid discharges. *Plasma Phys. Control. Fusion*, 54(9):095001, July 2012.

[33] C. D. Challis, J. Garcia, M. Beurskens, P. Buratti, E. Delabie, P. Drewelow, L. Frassinetti, C. Giroud, N. Hawkes, J. Hobirk, E. Joffrin, D. Keeling, D. B. King, C. F. Maggi, J. Mailloux, C. Marchetto, D. McDonald, I. Nunes, G. Pucella, S. Saarelma, and J. Simpson and. Improved confinement in JET high$\less$i$\greater$$\upbeta$$\less$/i$\greater$plasmas with an ITER-like wall. *Nucl. Fusion*, 55(5):053031, April 2015. Publisher: IOP Publishing.

[34] R. J. Dumont, J. Mailloux, V. Aslanyan, M. Baruzzo, C. D. Challis, I. Coffey, A. Czarnecka, E. Delabie, J. Eriksson, J. Faustin, J. Ferreira, M. Fitzgerald, J. Garcia, L. Giacomelli, C. Giroud, N. Hawkes, Ph Jacquet, E. Joffrin, T. Johnson, D. Keeling, D. King, V. Kiptily, B. Lomanowski, E. Lerche, M. Mantsinen, L. Meneses, S. Menmuir, K. McClements, S. Moradi, F. Nabais, M. Nocente, A. Patel, H. Patten, P. Puglia, R. Scannell, S. Sharapov, E. R. Solano, M. Tsalas, P. Vallejos, and H. Weisen and. Scenario development for the observation of alpha-driven instabilities in JET DT plasmas. *Nucl. Fusion*, 58(8):082005, June 2018. Publisher: IOP Publishing.

[35] M. Maslov, M. N. A. Beurskens, J. Flanagan, and M. Kempenaars. Note: Statistical errors estimation for Thomson scattering diagnostics. *Review of Scientific Instruments*, 83(9):096106, September 2012. Publisher: American Institute of Physics.

[36] Gary Taylor and Robert W. Harvey. Assessment of an Oblique ECE Diagnostic for ITER. *Fusion Science and Technology*, 55(1):64–75, January 2009. Publisher: Taylor & Francis _eprint: https://doi.org/10.13182/FST55-64.

[37] S. L. Prunty. A primer on the theory of Thomson scattering for high-temperature fusion plasmas. *Phys. Scr.*, 89(12):128001, November 2014. Publisher: IOP Publishing.

[38] E. de la Luna. Physics of ECE Temperature Measurements and Prospects for ITER. *AIP Conference Proceedings*, 988(1):63–72, March 2008. Publisher: American Institute of Physics.

[39] Katsumi Ida, Tatsuya Kobayashi, Mikirou Yoshinuma, Kenichi Nagaoka, Kunihiro Ogawa, Tokihiko Tokuzawa, Hideo Nuga, and Yuto Katoh. Direct observation of mass-dependent collisionless energy transfer via Landau and transit-time damping. *Commun Phys*, 5(1):1–9, September 2022. Number: 1 Publisher: Nature Publishing Group.